Nanoscale

ROYAL SOCIETY OF CHEMISTRY

PAPER

View Article Online
View Journal | View Issue



Cite this: *Nanoscale*, 2025, **17**, 12149

# 3D-printed kirigami-inspired asymmetric dressings: custom elasticity and self-pumping for enhanced wound healing†

Zhen Gu, * Siyang Cheng, Zhe Huang, Heng An, Liping Zhou* and Yongqiang Wen *

Received 31st December 2024,
Accepted 8th April 2025

DOI: 10.1039/d4nr05506c

rsc.li/nanoscale

Preventing infections and managing excessive exudate in dynamic joints are vital for effective wound treatment. Accurately fitting dressings to wound shapes remains a significant challenge, which can adversely affect both healing and patient comfort. This study introduces a self-pumping dressing with a tailored shape and tensile properties. This dressing channels excessive wound fluid in a unidirectional manner achieved by electrospinning hydrophobic nanofibers embedded with silver nanoparticles (AgNPs) onto a hydrophilic 3D-printed patch featuring a kirigami structure. By systematically adjusting the parameter-cutting length *l*, horizontal spacing *d*, and vertical spacing *h*, we enabled the elongation of the 3D-printed patch to range from 26% to 244%. Our personalized self-pumping dressings demonstrated effective antibacterial activity, unidirectional fluid transmission, and biocompatibility, thereby accelerating wound healing. This research establishes a promising pathway for personalized and precise local wound care.



## 1. Introduction

Skin serves as a protective barrier against external mechanical injuries and pathogenic invasions; however, it remains vulnerable to damage from external factors.[1,2] A breach in this protective barrier, whether due to a wound or disease, can lead to the overflow of tissue fluid, making it prone to endogenous (from skin tissues and mucous membranes) or exogenous (from bacteria in specific environments) invasions.[3] Effective management of wound fluid is crucial for effective wound treatment. The development of heterogeneous wetting composite films exhibiting unidirectional water permeability is a requirement.[4,5] This unique property is achieved through the strategic design of anisotropic wettability, utilizing gradients in wettability and structure to enable directional fluid transport while preventing reverse flow.[6,7] Building on this principle, electrospinning offers distinct advantages for unidirectional fluid transport and tissue repair applications.[8] Its ability to fabricate nanofibers that mimic the extracellular matrix provides precise control over fiber composition, diameter, and alignment, enabling the design of scaffolds that guide cell behavior such as adhesion, migration, and differentiation. Additionally, electrospun nanofibers can be tailored with gradient wettability to enhance fluid transport and promote tissue regeneration in complex anatomical regions, further broadening their potential for personalized medical applications.[9–11]

Yet, the predominant focus of unidirectional dressing research is primarily on static wound environments. Dressings for wounds near joints, which are subject to frequent move-

*Beijing Key Laboratory for Bioengineering and Sensing Technology, Daxing Research Institute, School of Chemistry & Biological Engineering, University of Science & Technology Beijing, Beijing 100083, China. E-mail: guzhen@ustb.edu.cn, Liping-Zhou@ustb.edu.cn, wyq_wen@ustb.edu.cn*

†Electronic supplementary information (ESI) available. See DOI: https://doi.org/10.1039/d4nr05506c

**Zhen Gu**

*Dr Gu is a lecturer at the University of Science and Technology Beijing (USTB) and a visiting scholar at the National University of Singapore. He received his Ph.D. from the Chinese Academy of Sciences and specializes in biointerface-based intelligent hydrogels for applications such as smart dressings and biomimetic microneedles. Dr Gu has published over 40 SCI-indexed papers, including Adv. Mater. and Sci. Adv., with 1700 citations and an H-index of 20. Recognized for his mentorship, he has received multiple awards and led over 10 research projects. His work has been featured in Science Net and Advanced Science News.*

ments, should ideally be flexible and extensible. In particular, in joints such as the elbow, finger, and wrist, wounds undergo compression or expansion due to body movements. Moreover, recent findings indicate that triboelectric or microneedle-based self-powered systems can complement these dynamic scenarios and promote wound healing through enhanced fluid transport and *in situ* electrical stimulation.[12,13] To address these challenges, 3D printing and kirigami-inspired designs offer transformative solutions.[14,15] 3D printing enables the precise fabrication of dressings with customizable mechanical properties and structures tailored to the specific geometry and dynamics of complex anatomical regions. It allows for the integration of multi-material constructs with spatial control, ensuring that dressings can flex and adapt seamlessly to joint movements while maintaining their functional integrity.[15,16] Meanwhile, kirigami-based designs, with their strategic incorporation of cuts and patterns, significantly enhance material stretchability, conformability, and deformability. These designs enable dressings to accommodate large strains and out-of-plane deformations, providing unparalleled flexibility and adaptability for high-motion areas like joints.[14,17] Recent research further demonstrates that such kirigami-based or layered composite constructs can expedite the re-epithelialization process *in vivo*, particularly when coupled with active wound modulation.[18,19] By combining these approaches, it becomes possible to develop wound dressings that not only meet the demands of dynamic environments but also expand the applicability of unidirectional transport systems to complex tissue repair scenarios.

In this study, we address the challenges associated with wound treatment in dynamic environments by developing a self-pumping dressing capable of unidirectional fluid transport and customizable mechanical properties. This dressing integrates electrospun hydrophobic nanofibers embedded with silver nanoparticles (AgNPs) for antibacterial efficacy with a 3D-printed hydrophilic patch featuring a kirigami-inspired structure to achieve tailored flexibility and extensibility (Fig. 1). By systematically adjusting the structural parameters, such as the cutting length, horizontal spacing, and vertical spacing, we tailored the elongation properties of the dressing to accommodate joint movements, expanding its applicability to high-motion areas such as the elbow and wrist. This approach not only enhances the adaptability of unidirectional transport systems but also provides a promising pathway for personalized and precise wound care, addressing the demands of complex tissue repair scenarios.

## 2. Materials and methods

### 2.1 Materials

Poly[4,4′-methylenebis(phenylisocyanate)-*alt*-1,4-butanediol/di(propylene glycol)/polycaprolactone] (PU) was obtained from Sigma-Aldrich (USA) for the preparation of the electrospun solution. Silver nitrate ($AgNO_3$) was sourced from Beijing Chemical Works (China). Fluorescein sodium salt and *N*,*N*-dimethyl formamide (DMF) were purchased from Aladdin Industrial Corporation (China). E-Denstone peach, which is a yellow light-cured methacrylic acid/acrylic resin, was purchased from EnvisionTEC GmbH (Germany). Isopropanol (IPA) from Macklin Biochemical Corporation (China) was used as a cleaning agent for light-cured resin. The hydrophilic reagent (HR) was obtained from the Institute of Zoology, Chinese Academy of Sciences (China). *Escherichia coli* O157:H7 (ATCC 25922) and *Staphylococcus aureus* (ATCC 6538) were provided by the American Type Culture Collection (USA). NIH/3T3 medium purchased from Procell (China) was used for culturing NIH/3T3 (Procell). A Calcein/PI Live/Dead Viability/Cytotoxicity Assay Kit was sourced from Beyotime Biotechnology (China). Methyl thiazolyl tetrazolium (MTT) was obtained from Beijing Solarbio Co. Ltd (China). All reagents were used as received.

### 2.2 Preparation of hydrophobic nanofiber membranes

Hydrophobic nanofiber membranes were created *via* electrospinning. PU was dissolved in DMF (PU/DMF = 12.5 wt%) with stirring overnight to obtain a uniform precursor solution. The uniform PU precursor was divided into two parts, marked as P1 and P2. About 2 mL of the precursor solution was drawn from P1 into a 20 mL syringe equipped with a stainless-steel needle of 22 G. P1 was discharged using a digitally controlled syringe pump and the flow rate was set at 2 mL $h^{-1}$. The experiment was conducted at 25 °C with 25% relative humidity and a 15 cm receiving distance. The application voltages were set to 20 kV, 25 kV, and 30 kV for 2 min and the fibers were collected with aluminum foil. PU nanofiber membranes with AgNPs (PU-A) were prepared as previously reported.[20] The electrospinning solution containing AgNPs was prepared by adding 2% $AgNO_3$ to the above prepared P2 and stirring at room temperature for 4 h. The voltages between the needle and the electrodes were set as 20 kV, 25 kV and 30 kV, the other condition parameters remain unchanged, and the electrospinning time was set as 2 min. Finally, keeping other conditions unchanged, the most suitable spinning voltage was selected according to the comprehensive characterization results, the electrospinning solution containing AgNPs was electrospun, and the electrospinning time was set as 2 min, 4 min, 6 min and 8 min, respectively.

### 2.3 Preparation of the personalized hydrophilic patch with large deformation based on 3D printing (PH3D)

Patterned patches were printed with a desktop DLP 3D printer (EnvisionTEC GmbH, Gladbeck, Germany). The printer uses an inverted stereolithographic process, emitting the laser beneath the resin tray to construct the object layer by layer from the bottom up. The size of the built platform is 45 × 28 × 100 mm. The XY resolution is 25 μm with a theoretical layer thickness of at least 50 μm in the *Z* direction. All PH3D models were created using 3D Max 2016 software (Autodesk). Table 1 lists the size parameters of the PH3D samples, including the cutting length *l*, horizontal spacing *d*, vertical spacing *h*, and overall size. The STL file format was imported into the compatible slicing software (Perfactory Software Suite Administration

 

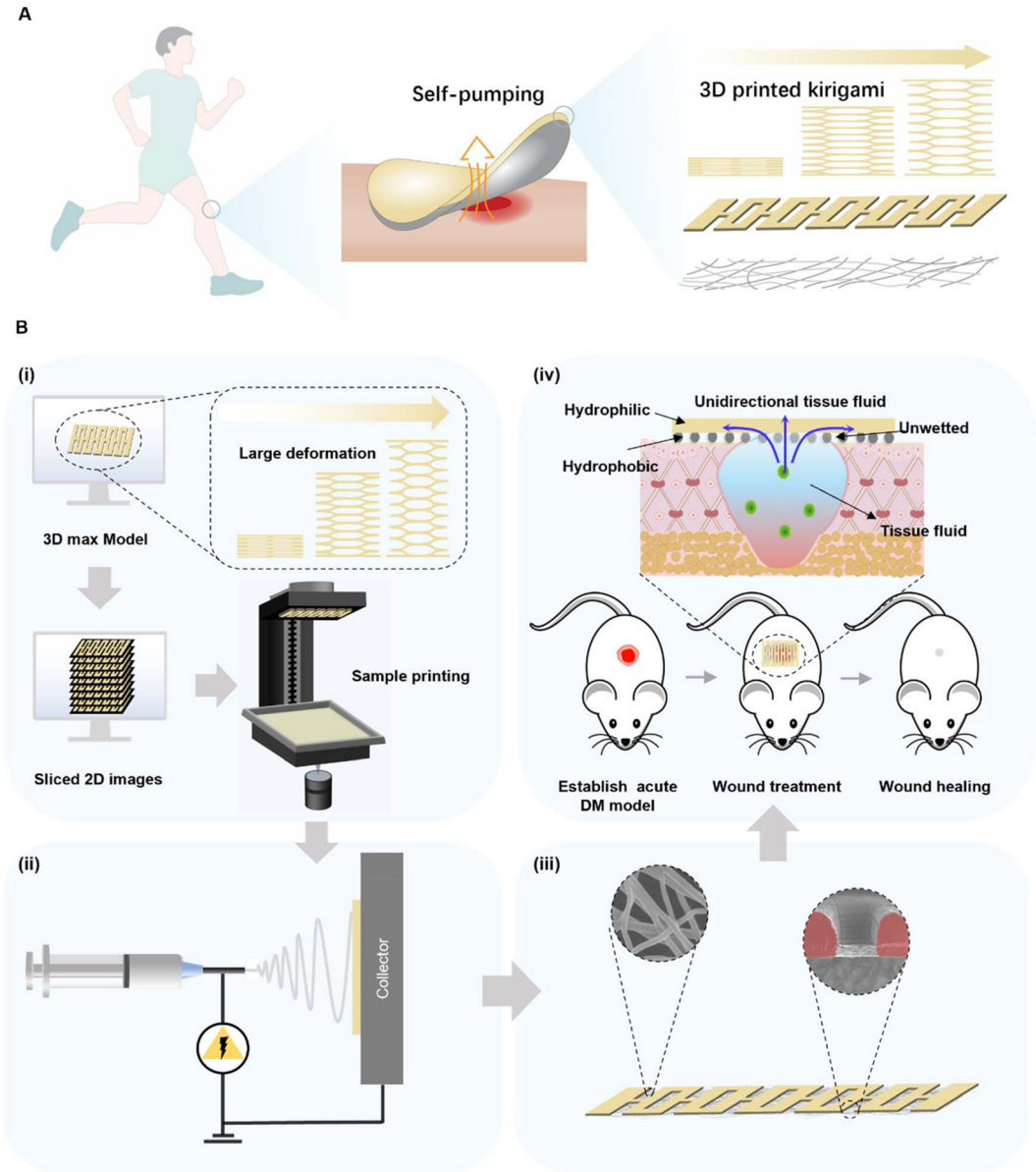


**Fig. 1** Development and application of customized self-pumping dressings with large deformation. (A) Illustration of the self-pumping dressing combining a 3D-printed kirigami-inspired structure and hydrophobic nanofibers designed for dynamic wound environments such as joints. (B) (i) Schematic illustrating the preparation of the personalized hydrophilic patch with large deformation based on 3D printing (PH3D). The process begins with designing the patch using 3D modeling software (*e.g.,* 3D Max), where the patch structure is tailored to achieve large deformation properties. The 3D model was then sliced into 2D images and sent to the DLP-based 3D printing system for fabrication. This approach ensures precise customization of the patch's geometry and mechanical properties. (ii) Electrospun PU with AgNP nanofibers (PU-A) onto the PH3D base. (iii) PH3D@PU-A bilayer showing self-pumping capabilities. Insets: scanning electron microscopy (SEM) images of the PU-A nanofiber and a cross-section of the bilayer dressing. (iv) Application of the tailored bilayer self-pumping dressing on mouse wounds.

Guide Version 3.2, EnvisionTEC, Germany) matched with the printer. The software locates the preformed model and sets the resolution of the printed patch. After setting these parameters, the software slices the patch model layer by layer before sending the dedicated folder to the printer. The resin patches were washed in an isopropanol (IPA) bath for 5 min. The residual raw resin on the patch surface was removed using an air-blowing bottle (OPULA, China) and this process was repeated twice. After washing, the patches were placed in an ultraviolet curing device (FormCure, FormlabsInc, USA) for secondary curing, the temperature and time were set to 25 °C and 2 min, and the personalized patches with large deformation based on 3D printing (P3D) were successfully obtained. The P3D samples were soaked in an HR/IPA (v:v = 7 : 3) mixed reagent and soaked evenly for 1 min. Then, we obtained blow-dried PH3D with a high-pressure air gun.

Table 1 Design parameters for nine PHP samples

| Patch number | $l$ (mm) | $d$ (mm) | $h$ (mm) | Cell count |
|---|---|---|---|---|
| $l$-I | 8 | 3.2 | 0.25 | 10 |
| $l$-II | 12 | 3.2 | 0.25 | 10 |
| $l$-III | 16 | 3.2 | 0.25 | 10 |
| $d$-I | 8 | 3.8 | 0.25 | 10 |
| $d$-II | 8 | 3.5 | 0.25 | 10 |
| $d$-III | 8 | 3.2 | 0.25 | 10 |
| $h$-I | 8 | 3.2 | 0.35 | 8 |
| $h$-II | 8 | 3.2 | 0.3 | 8 |
| $h$-III | 8 | 3.2 | 0.25 | 8 |

### 2.4 Preparation of a bilayer self-pumping wound dressing

The PH3D was attached to the flat aluminum foil of the electrospinning device with double-sided adhesive. A PU electrospinning solution with AgNPs was prepared. The electrospinning solution was drawn into a 20 mL syringe with a 22 G stainless steel needle at a flow rate of 2 mL $h^{-1}$. The experiment was conducted at 25 °C, with 25% relative humidity, 15 cm receiving distance, and 25 kV application voltage. Spinning times were set as 2 min, 4 min, 6 min and 8 min. After electrospinning, the composite bilayer self-pumping dressing was removed using a blade and dried for 2 h in a vacuum furnace (ZHONGKEBODA, DZF-6020, China) at 50 °C. The film was regarded as a PH3D@PU-A bilayer self-pumping dressing.

### 2.5 Characterization of PU nanofibers, PU-A nanofibers, PH3D and the PH3D@PU-A bilayer self-pumping dressing

**2.5.1 SEM and TEM.** The samples' morphological characteristics were analyzed using a scanning electron microscope (SEM, HITACHI, SU-8010, Japan) and a transmission electron microscope (TEM, HITACHI, HT7700 Exalens, Japan). The sample was coated with an ion sputter coater (HITACHI, MC1000, Japan) before SEM imaging. The average diameter and distribution of the nanofibers were determined by measuring the diameters of at least 50 fibers using ImageJ software (National Institutes of Health in Bethesda, Maryland, USA).

**2.5.2 Water contact angle (WCA).** The hydrophilicity and wettability of different samples were measured at room temperature using a water contact angle (WCA) system (Data Physics, OCA ESr, Filderstadt, Germany). Two microliters of deionized water were dripped onto the surfaces of different samples, the time of droplet infiltration was recorded by video surveillance, and the contact angle was measured from the captured images. Each recorded contact angle was averaged from at least six independent measurements.

**2.5.3 Measurement of the hydrostatic pressure.** The hydrostatic pressure testing device, custom-designed by the Technical Institute of Physics and Chemistry CAS, has two sample nesting cavities and a tubular container. The special cavity for slicing was sized to match the resin sheet and customized elastic dressing. The special cavity design for the nanofibers requires good air tightness but not strict size specifications. The tubular container was 30 cm long with a 17 mm inner diameter. The hydrostatic pressure was measured by fixing sample surface areas, dripping water slowly into a tubular container, and recording the maximum height of the water column at penetration. Three independent experiments were conducted.

**2.5.4 Antimicrobial test.** The antibacterial activity of the PU-A nanofibers was assessed using the colony counting method. Two model bacterial colonies were grown in Luria–Bertani (LB) medium at 37 °C for 24 h. The inoculum was diluted to $1 \times 10^6$ CFU $mL^{-1}$. A series of PU-A nanofibers with cut specifications of 7 mm × 7 mm were added to the bacterial suspension and incubated in a shaking flask incubator at 37 °C for 24 h. Then, 100 μL of bacterial suspension was spread in a Luria–Bertani Agar plate and incubated at 37 °C for 24 h. The colonies were evaluated using an automatic colony counter (Supcre G9, Shineso, Hangzhou, China). Three tests were conducted in each group. The bacterial inhibition rate (%) was calculated using eqn (1):

$$\text{Inhibition rate}\,(\%) = \frac{M_0 - M_1}{M_0} \times 100 \quad (1)$$

where $M_0$ is the number of control groups of bacterial colonies and $M_1$ is the number after sample addition.[21] Each experiment was repeated three times, with data expressed as the mean ± standard deviation (SD).

**2.5.5 Mechanical test of PH3D.** The tensile properties of nine patch groups were measured with an ESM303 tensile tester (MARK-10, USA). The samples were clamped vertically with a non-slip clamp to minimize slippage errors. A 10 N piezoelectric load cell was used to measure the tensile load at a velocity of 20 mm $min^{-1}$. A digital camera (EOS90D, Canon) was used to record the patch's state during stretching for later use of digital images. The tests were repeated six times to calculate averages and standard deviations.

**2.5.6 Investigation of the unidirectional biofluid excretion performance of dressings in a simplified exudative wound model.** Firstly, the self-pumping wound dressing was placed horizontally on a U-shaped platform according to both self-pumping directions. Secondly, a syringe connected to an injection pump (SPLab10, SHENCHEN, China) was placed on the dressing to continuously supply fluorescein-labeled FBS (1% fluorescein sodium) at 80 μL $min^{-1}$. Finally, the flow track of fluorescence-labeled FBS was recorded with a digital camera (EOS90D, Canon, Japan) under ultraviolet light ($\lambda$ = 254 nm). To more accurately simulate the direction of the tissue fluid pumped out of the wound, the dressing was placed on a solid U-shaped bench along the self-pumping direction, the whole was inverted, and a syringe was placed under the dressing to record the self-pumping performance of fluorescence-labeled FBS under ultraviolet light in the same way.

**2.5.7 *In vitro* biocompatibility assay.** The biocompatibility of PH3D@PU-A dressing on NIH3T3 cells was evaluated using the MTT method. The NIH3T3 cell line was sourced from the Cell Bank of Beijing, Chinese Academy of Sciences (Beijing, China). Briefly, the cells were inoculated at 37 °C and cultured in a 96-well plate for 24 h. Then a fresh medium containing

 

different final concentrations of PH3D@PU-A was used instead of the culture medium at 37 °C for 24 h. Finally, MTT reagent was added to each well and cultured for 4 h. The absorbance at 570 nm was measured using a microplate reader (Model 680, BIO-RAD, USA). The MTT results were validated by the live/dead assay (Calcein AM/PI Double Stain Kit, Yeasen, China). The cell suspension was mixed with the staining solution, incubated at 37 °C for 15 min per the manufacturer's instructions, and observed with a laser scanning confocal microscope (Olympus FV1000, Japan).

**2.5.8 Establishment of the wound healing model *in vivo*.** A 0.5 cm circular wound was created by excising the dorsal area of the mice. The C57BL/6 mice were divided into three groups: exposed wound control (i), PU-A-13.3 nanofiber (ii), and PH3D@PU-A-13.3 self-pumping dressing (iii). The anterior and posterior ends of the dressings were fixed using adhesive bandages (i) and the dressings were changed every 3 d (ii). Photographs of skin trauma were taken on days 0, 7, and 14, respectively, and the skin trauma area was measured using Image J software. The relative wound area (%) was calculated using eqn (2).

$$\text{Relative wound area}\,(\%) = \frac{S_t}{S_0} \times 100\% \quad (2)$$

where $S_t$ and $S_0$ denote the wound area on day $t$ and day 0, respectively. Each experiment was repeated three times for all groups, with data expressed as the mean ± standard deviation (SD).

**2.5.9 Histological staining.** Mice were euthanized on day 14 for histological analysis. Cuts were made at the wound bed and healthy skin, and some newborn tissue was collected. Tissue samples were fixed in 4% paraformaldehyde for 3 days, dehydrated in ethanol (30%, 50%, 60%, 70%, 90%, and 100%), and embedded in resin. Following resin block fixation, tissues were sectioned to 5 μm with an optimal cutting temperature compound (Sakura Finetek, Torrance, CA, USA). Samples were stained with hematoxylin and eosin (H&E) (Solarbio, China) and Masson trichrome (Solarbio, China). The stained slides were analyzed. Quantitative analysis was performed with ImageJ software.

### 2.6 Statistical analysis

Experiment data were analyzed using Origin 8.5. Statistical analysis was performed using SPSS 25. Differences between two groups were analyzed with *t*-tests and differences among multiple groups were assessed using one-way ANOVA with Tukey's *post hoc* test. Values are shown as the mean ± S.D. A value of $p < 0.05$ was used to indicate statistical significance.

## 3. Results

### 3.1 Effect of spinning voltage and AgNP doping on the nanofiber morphology

We prepared PU nanofibers using a 12.5 wt% PU solution without AgNPs to investigate the effects of spinning voltage and AgNP doping on their morphology. The morphologies of the PU nanofibers prepared at different applied voltage parameters (20 kV, 25 kV, and 30 kV) are shown in Fig. 2A–C. At a 20 kV applied voltage, the PU nanofibers had low spinning efficiency and an irregular shape, and beads with larger diameters could be clearly observed on the fiber surface. At 25 kV, the electric field force on the droplets increased, resulting in a stable jet that enabled the end of the spinneret became larger, and then the droplets gradually formed a relatively stable jet, which provided conditions for ejecting fibers with good morphology. The resulting fiber had a smooth surface, uniform diameter, irregular orientation, and no extra beads. At 30 kV, the nanofiber spinning efficiency was high, but a few beads formed. High voltage accelerated the charged fiber, causing the unstable fluid to exit the spinneret quickly and resulting in poor fiber shape. Under the same spinning conditions but different voltages (20 kV, 25 kV, and 30 kV), three groups of PU nanofibers doped with 2% AgNPs (from $AgNO_3$)[22] were prepared, which was marked as PU-A. The effect of different applied voltage parameters on the morphology of PU-A can be seen from Fig. 1D–F. At the voltage of 20 kV, although the diameter distribution of the PU-A nanofibers was more uniform (Fig. S1A†) than that of the PU nanofibers, the filament yield was still low and the bead-like structure with smaller diameter could be clearly seen. At spinning voltages of 25 kV and 30 kV, the PU-A nanofibers displayed a regular morphology, smooth surfaces, disordered orientation, and uniform diameter distribution, with minimal bead formation (Fig. S1B and C†). The addition of 2% $AgNO_3$ to the spinning solution formed AgNPs, consuming $Ag^+$ ions and producing $H^+$ ions, which improved the fluidity and electrical conductivity.[23] The increase of electrical conductivity led to a stronger pulling force of the spinning solution under the same electric field, which increased the spinnability of the solution, and the resulting fiber has a more regular morphology and more uniform diameter distribution.[24] By comparing the fiber morphology images before and after doping silver nanoparticles, it can be determined that the existence of silver nanoparticles had little effect on the change of fiber morphology (Fig. 2B and E). We selected the PU-A nanofiber prepared at 25 kV to ensure fiber shape and quality for further experiments.

### 3.2 Performance characterization of the hydrophobic PU-A layer

Previous studies have shown that the unidirectional transport function of hydrophilic/hydrophobic composite membranes has no strict requirement on the thickness of the hydrophilic layer and the thickness of the hydrophobic layer plays a key role in the transport characteristics of liquid membranes.[25] Thicker hydrophobic fiber layers slowed the liquid transfer from the hydrophobic end to the hydrophilic end, which was the source of the supporting layer and pumping force. When the thickness reaches a critical value, liquid retention causes the unidirectional transport function to fail.[6] Therefore, the thickness of the hydrophobic fibers can be adjusted by controlling electrospinning time, enabling the study of synergistic

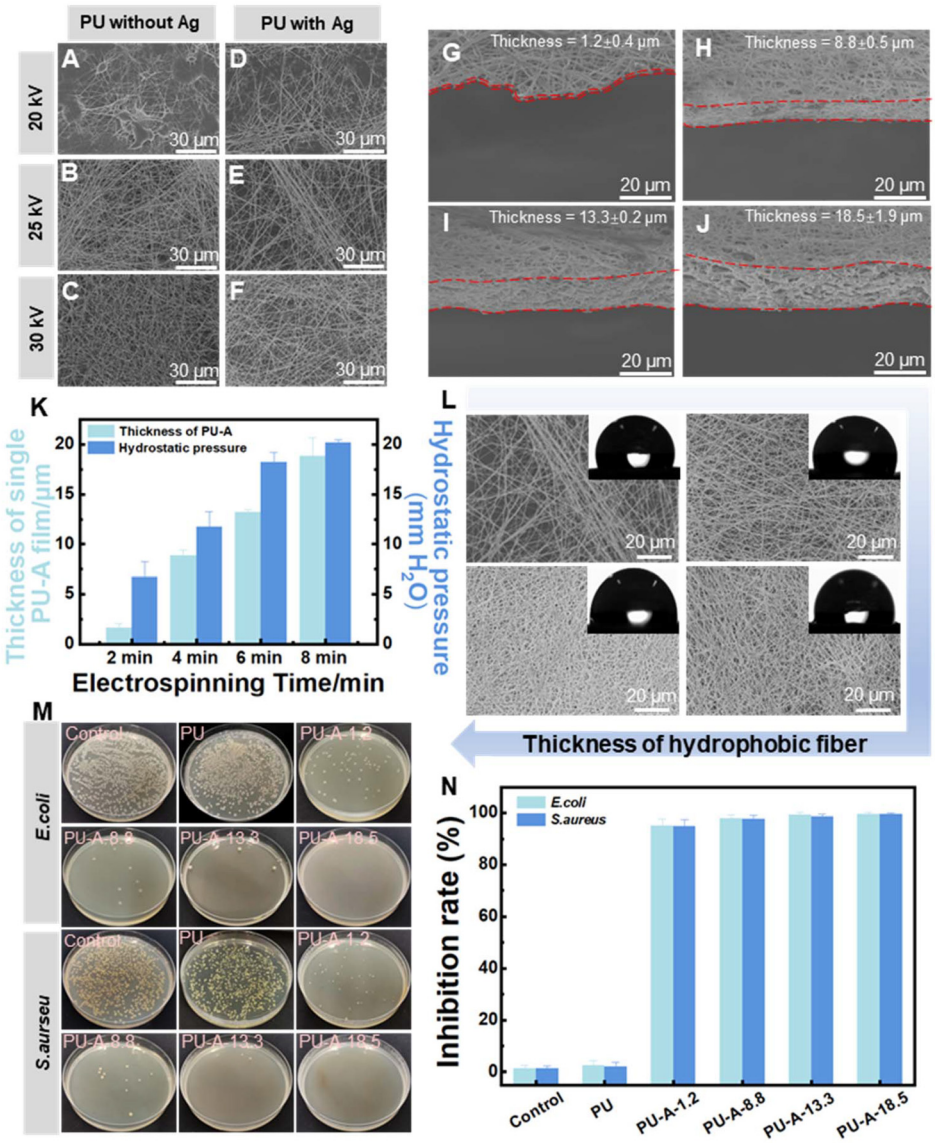


**Fig. 2** Morphology and properties of the hydrophobic PU and PU-A nanofiber membranes. SEM image of the surface morphology of PU without AgNPs (A–C) and PU with AgNPs (D–F) under various applied voltages of 20 kV, 25 kV and 30 kV; cross-sectional images of four PU-A nanofibers, which were prepared by spinning at 2 min (G), 4 min (H), 6 min (I), and 8 min (J); (K) relationship of the electrospinning time (2, 4, 6, and 8 min) *versus* the thickness of PU-A and hydrostatic pressure (HP); (L) optical images of water droplets on the hydrophobic PU-A nanofibers of different thicknesses; (M) antibacterial activities against *E. coli* and *S. aureus*; and (N) inhibition rates for *E. coli* and *S. aureus*. Values are shown as the mean ± s.d. ($n$ = 3) indicated by error bars.

effects between the hydrophobic and hydrophilic layers in unidirectional water transport. Four groups of PU-A nanofibers with thicknesses of 1.2, 8.8, 13.3, and 18.5 μm were prepared by spinning for 2, 4, 6, and 8 min (Fig. 2G–J). They were designated PU-A-1.2, PU-A-8.8, PU-A-13.3, and PU-A-18.5. The hydrostatic pressure (HP) was measured to assess water pressure through the hydrophobic PU-A nanofibers. Fig. 2K shows the relationship between the electrospinning time, the fiber film thickness, and the HP. Increasing PU-A thickness led to higher hydrophobic permeability (HP) due to longer hydrophobic channels that hinder water penetration. We studied the wetting behavior of water droplets on the hydrophobic PU nanofibers of different thicknesses (Fig. 2L). When 2 μL of water droplets were applied to the low-thickness hydrophobic PU-A-1.2, some passed through the nanofiber membranes (CA ≈ 110°). Increasing the thickness of hydrophobic nanofibers increased the fiber density, making water droplets harder to penetrate and creating a flatter spherical bottom. The contact angle of water droplets decreased from 110° to 100° (Fig. S2A†). Fetal bovine serum (FBS) and bacterial solutions simulated biological tissue to characterize the PU-A-1.2 nanofibers. The results showed that their membrane permeation effect was similar to that of water droplets (Fig. S2B†). Controlling the fiber thickness allows regulation of hydro-

 

phobic PU-A permeability, facilitating directional tissue fluid delivery from the pump dressing. The hydrophobic layer of the self-pumping dressing is applied to injured skin to remove excess fluid and offer antibacterial protection. The hydrophobicity of PU-A nanofibers did not change compared to pure PU nanofibers (Fig. S3†). The transmission electron microscopy (TEM) image showed uniform AgNPs on the PU-A fiber surface, averaging 13.5 ± 0.4 nm in diameter (Fig. S4†). Silver nanoparticles (AgNPs) have a high surface area that inhibits bacterial enzyme activity and disrupts membrane structures.[26] The antibacterial activity of PU-A at different thicknesses was evaluated using colony counting. Fig. 2M shows that many colonies formed on agar plates without AgNPs in the fibrous membrane. In Agar plates co-cultured with PU-A, the surface bacteria decreased with a longer spinning time of PU-A. There were no colonies on the PU-A-18.5 agar plate. As shown in Fig. 2N, the inhibition rates of the four PU-A were more than 94%, demonstrating that the attached AgNPs effectively inhibited the survival of Gram-negative *E. coli* and Gram-positive *S. aureus*. The PU-A hydrophobic layer with 2% AgNPs demonstrated strong antibacterial properties, essential for the ideal self-pumping dressing.

### 3.3 Preparation and characterization of the hydrophilic large deformation layer

While hydrophobic PU-A dressings have potential for unidirectional transport of wound fluid, they are primarily used on static wounds.[27,28] Most of the skin injuries caused by falls, bumps and other accidents occurred in the position of joint activity and the traditional static dressing only has a small ultimate tensile strain of 10–20%, which was not enough to meet the treatment needs of joint wounds with a large telescopic scale. Inspired by kirigami structures, 3D printing technology with adjustable parameters was used to create customized tensile properties, expanding the application range of personalized self-pumping dressings. Large deformation (LD) layers were created using DLP-based 3D printing technology (Fig. 3A). Fig. 3B depicts a kirigami structure with a central rectangular arrangement of patterned lines made up of vertically distributed units in series. Theoretically, by adjusting the cutting length $l$, horizontal spacing $d$ and vertical spacing $h$ in the unit body, the patch with ideal tensile properties could be customized.[29] We created nine patch groups with different parameters to assess the customizability of their tensile properties (Table 1). Kirigami extension states are shown in Fig. 3C–E. When the kirigami structure was stretched, all cutting elements buckled out of plane. As the retractable area deformed, the planar notch opened and showed horizontal shrinkage. The analysis of groups $l$, $d$, and $h$ revealed that $h$-III in group $h$, $d$-III in group $d$ and $l$-III in group $l$ showed the minimum critical buckling force and the highest elongation, respectively. The breaking elongation percentages for $h$-III, $d$-III, and $l$-III were 45%, 100%, and 244%, respectively (Fig. 3F–H). The degree of deformation of the stretchable planar notch in LD increases with lower $h$, lower $d$, and higher $l$, making elastic deformation easier. Young's modulus indicates the ability of the material to resist elastic deformation and the inverse relationship between elongation at break and Young's modulus further verified that the elasticity of LD can be regulated regularly by adjusting the $h$, $d$, and $l$ parameters (Fig. 3I–K). Thus it could be seen that by setting the $h$, $d$, and $l$ parameters of the patch respectively on the computer, it was like rotating the "gear" to adjust the elastic strength of the patch, in which the elastic range of "$l$ gear" was the largest, which was recorded as the big "gear". The "$d$ gear" and "$h$ gear" were classified as the medium and small gears. Properly adjusting these "gears" allows for the design of a patch with ideal elastic performance, facilitating the realization of the LD.

In view of the fact that there were great differences in the flexibility and bending range of joints in different parts of the human body and there was a lack of the literature on the mechanical properties of dressings for different joints in the field of wound repair; therefore, this study selected the LD which could show the maximum elongation at break as the next research in order to meet the comfort of most human joints. The LD must be hydrophilic to prepare personalized stretch self-pumping dressings with asymmetric wettability. The LD demonstrated stable hydrophilic properties after a 3 min treatment confirmed by the infiltration behavior of resin slices (Fig. S5†). Prior to hydrophilic treatment, the droplet was diffused for 30 seconds without wetting the LD surface (Fig. S6A†). After hydrophilic treatment, LD slices were fully wetted in 0.5 seconds of dynamic liquid spreading (Fig. S6B†). The hydrophilic resin chip's small, uniformly distributed gaps and strong capillary effect enabled rapid and even liquid diffusion on its surface. The hydrophilic LD allows the self-pumping dressing to efficiently pump tissue fluid.

### 3.4 Characterization of the unidirectional transmission performance of self-pumped large deformation custom dressings

In order to further understand the water transport behavior of self-pumped large deformation custom dressings, LD@PU-A double-layer self-pumping dressings with different thicknesses of hydrophobic layers were prepared at different spinning times (2, 4, 6 and 8 min), which were recorded as LD@PU-A-1.2, LD@PU-A-8.8, LD@PU-A-13.3, and LD@PU-A-18.5, respectively. Fig. 4A illustrates that the LD and PU-A nanofibers intertwined at the contact interface, enhancing the water transport speed and enabling unidirectional liquid movement. Fig. 4B depicts the moisture transfer process of four LD@PU-A bilayer self-pumping dressings. When the liquid drops to the hydrophobic side, the four kinds of LD@PU-A double-layer dressings with hydrophilic/hydrophobic wettability showed good hydrophobic properties, that is the WCA of water droplets on the surface of the dressing was more than 100°. As the electrospinning time increases and the hydrophobic layer of PU-A thickens, the wetting time of the double-layer self-pumping dressing also increases, recorded as 0.410 s, 1.1 s, 1.875 s, and 9 s. The hydrostatic pressures of the self-pump direction (positive direction) and the reverse self-pump direction (reverse direction) were also measured

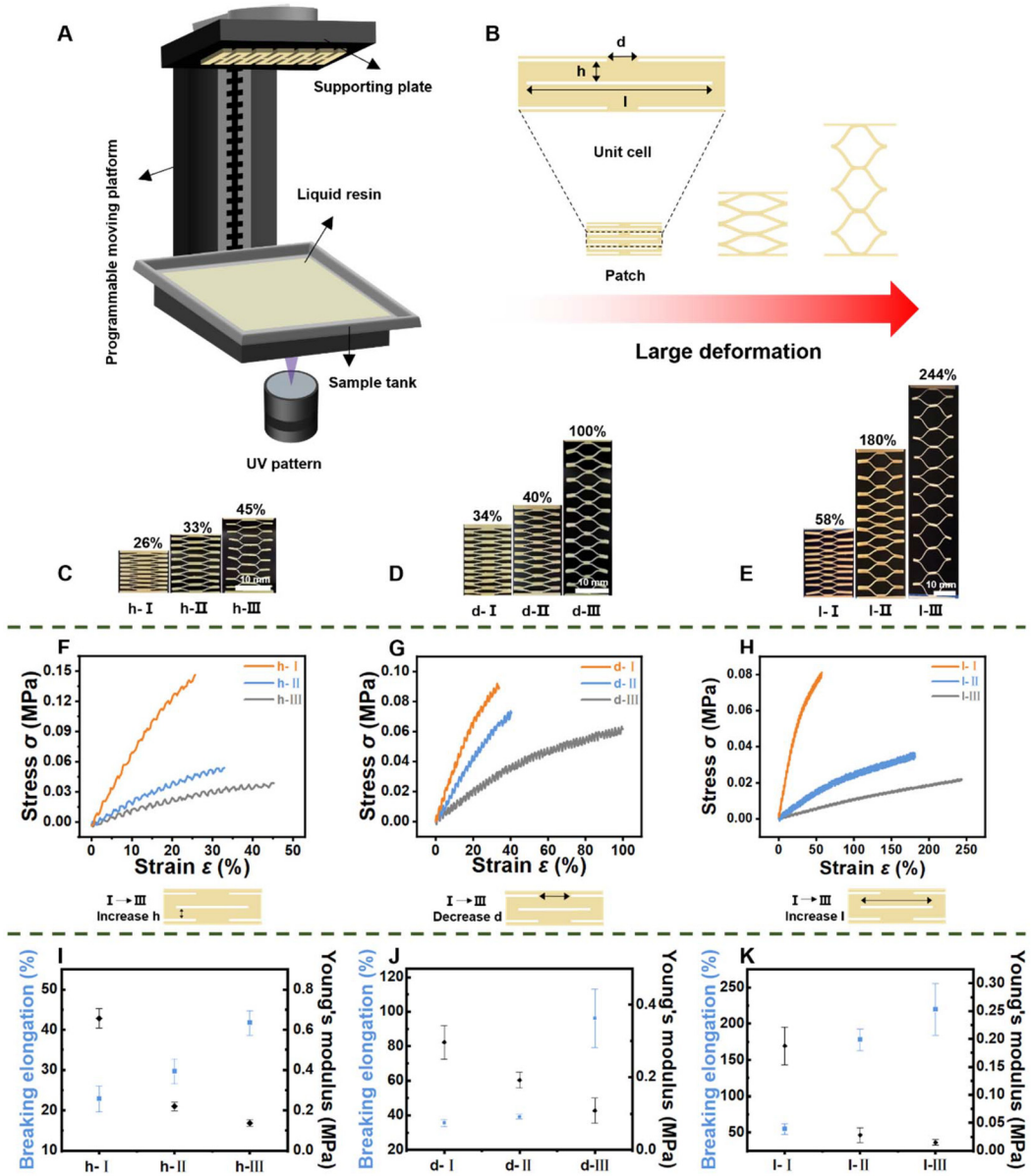


**Fig. 3** Characterization of PH3D's printed structure and mechanical properties. (A) Scheme of the experimental setup for the DLP 3D printing process; (B) typical kirigami structural unit of LD and its stretching schematic diagram; photographs of three sets of LD (*n*-I, *n*-II, and *n*-III, where *n* is *h*, *d* or *l*) at maximum strain for changing only the parameters *h* (C), *d* (D) or *l* (E); tensile stress–strain curves (F) and breaking elongation–Young's modulus scatter plots (I) for LD under the conditions of changing only the parameter *h*; tensile stress–strain curves (G) and breaking elongation–Young's modulus scatter plots (J) for LD under the conditions of changing only the parameter *d*; and tensile stress–strain curves (H) and breaking elongation–Young's modulus scatter plots (K) for LD under the conditions of changing only the parameter *l*.

(Fig. 4C). The increased thickness of the hydrophobic layer increased, leading to the hydrostatic pressure of the corresponding dressings in reverse self-pumping direction increased slowly. The hydrostatic pressures in the reverse direction were 6.26 ± 1.8 mm $H_2O$, 12.13 ± 1.4 mm $H_2O$, 18.82 ± 2.3 mm $H_2O$, and 19.70 ± 2.4 mm $H_2O$, respectively. However, they are still much lower than the hydrostatic pressures in the positive direction, which were 0.28 ± 0.03 mm $H_2O$, 0.59 ± 0.35 mm $H_2O$, 0.95 ± 0.43 mm $H_2O$, and 3.50 ± 0.75 mm $H_2O$, respectively. The difference between the forward and reverse hydrostatic pressures of the corresponding dressing was used to show the strength of pump action of the hydrophilic resin layer in the unidirectional output of the liquid and the corresponding average values were 5.98 mm $H_2O$, 11.54 mm $H_2O$, 17.87 mm $H_2O$ and 16.2 mm $H_2O$, respectively. Therefore, we chose LD@PU-A-13.3 as the material for follow-up self-pump macroscopic characterization and animal experiments, because it provided the maximum drainage capacity to reduce the hydrostatic pressure of the dressing, namely the maximum capacity of pumping tissue fluid. The hydrostatic pressures of

 

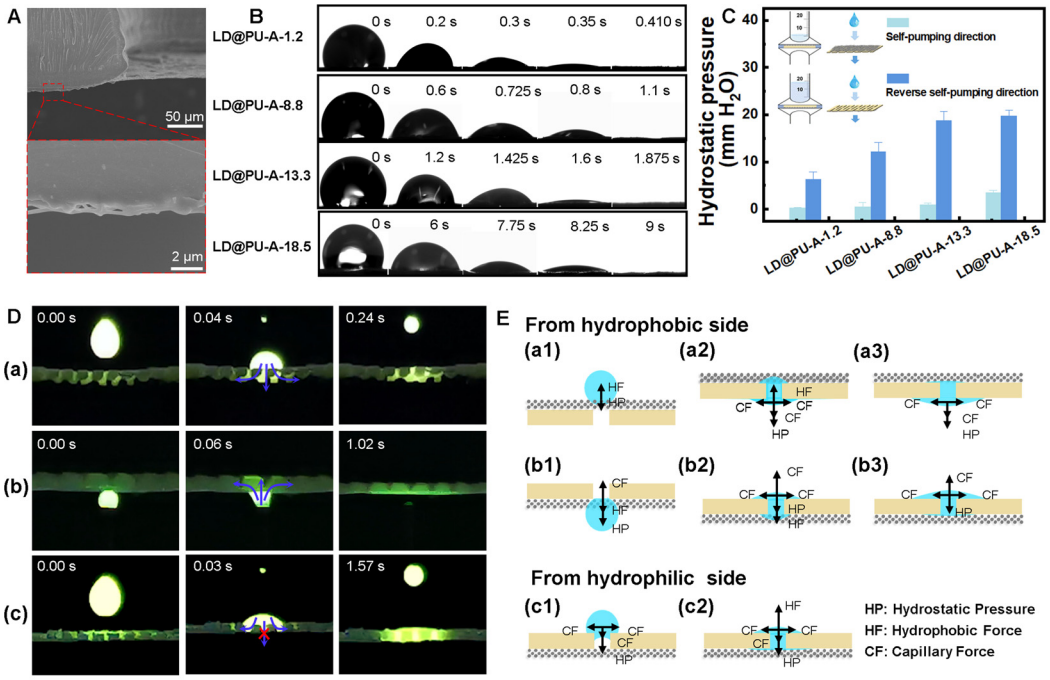


**Fig. 4** Demonstration of unidirectional fluid transport in the PH3D@PU-A bilayer self-pumping dressing. (A) Cross-sectional SEM image of the LD@PU-A double-layer self-pumping dressings. The magnified section (red inset) shows the well-bonded structure of the two layers; dynamic WCA variation (B) and anisotropic hydrostatic pressure (C) of the LD@PU-A double-layer self-pumped dressings with different hydrophobic layer thicknesses. The inset shows the liquid drip addition directions, both in the self-pumping direction and in the inverse self-pumping direction; and (D) images of the interaction of droplets (labeled with 1% sodium fluorescein) with the LD@PU-A double-layer self-pumping dressing under UV light irradiation ($\lambda$ = 254 nM). Downward (a) and upward (b) drops are applied to the dressing, moving liquids from the hydrophobic to the hydrophilic end. Downward (c) droplets fall onto the dressing in the reverse self-pumping direction, not passing through the hydrophobic layer. The blue arrows show the droplet flow direction in the dressing and the red X indicates that the liquid retention. (E) Schematic diagram of the directional water transfer mechanism. (a1–a3) Droplets falling onto the hydrophobic surface and being transported to the hydrophilic layer driven by hydrostatic pressure (HP) and capillary force (CF); (b1–b3) droplets injected from below and migrating through the hydrophobic layer to the hydrophilic side under the combined action of CF, HP, and hydrophobic resistance (HF); (c1–c2) droplets failing to penetrate from the hydrophilic side due to insufficient force to overcome HF, resulting in liquid retention.

the four double-layer dressings in the reverse self-pumping direction were similar to those of the four groups of the same thickness (Fig. S7†). The self-pumping dressing after composite LD minimally affects the micro-pore size and porosity of the hydrophobic nanofibers, meeting the required functional standards. Dynamic WCA measurements (Fig. S8†) further revealed that increasing the elongation ratio of the dressing from 0% to 200% reduced the droplet infiltration time from 1.15 s to 0.46 s, demonstrating enhanced fluid transport efficiency under mechanical stretching.

We created a simplified exudative wound model to demonstrate the fluid direction capability of the LD@PU-A self-pumping dressings. The syringe with the green FBS solution (1% sodium fluorescein) was held vertically and droplets were evenly applied to the dressing. Under UV radiation ($\lambda$ = 25.4 nm), we observed the dynamic draining process of green FBS solution on the self-pumping dressing (Movies S1 and S2, ESI†). The dressing infiltration using reverse self-pumping served as a control (Movie S3, ESI†). When the green FBS solution was dropped downward or injected upward along the direction of the self-pumping of the dressing, the droplet first makes contact with the surface of the hydrophobic layer of the dressing and then quickly passed through the hydrophobic layer and infiltrated the hydrophilic layer (Fig. 4D(a) and (b)). When the green FBS solution is dripped in the reverse self-pumping direction, droplets first contact and quickly infiltrate the hydrophilic layer of the dressing. The hydrophobic layer restricts the droplets to spreading parallel to the hydrophilic layer (Fig. 4D(c)). The results show that with the continuous and stable dripping of green FBS solution, the LD@PU-A dressing could transport the simulated exudate from its hydrophobic side to its hydrophilic side, but it not be transported in the opposite direction, so as to achieve the purpose of transporting liquid in one direction.

We proposed a mechanism to explain the dressing's unidirectional fluid output based on these results. As shown in Fig. 4E(a1), when a water droplet drips on the surface of the PU-A hydrophobic layer, it initially presented a Wenzel–Cassie state and was subjected to two forces in the opposite direction, namely hydrophobic (HF) and hydrostatic pressure (HP).[30,31] For a specific hydrophobic film, HF played a role in preventing liquid penetration, which was usually a fixed value. Hydrostatic pressure (HP) is considered the reason for the unidirectional liquid transfer in self-pumping dressings pro-

portional to the droplet height.[25] When the droplet's force on the hydrophobic film meets HF < Hp, it passes through the hydrophobic layer and contacts the hydrophilic layer. Capillary forces (CF) and HP in the hydrophilic layer work together to resist HF, promoting water soaking and diffusion, as shown in Fig. 4E(a2). Finally, droplets pass through the hydrophobic layer and diffuse into the hydrophilic layer due to CF and HP until the hydrophobic layer becomes dry (Fig. 4E(a3)). As shown in Fig. 4E(b1), When the upward injected droplets horizontally make contact with the surface of the PU-A hydrophobic layer, the force on the droplets satisfies HF + HP < CF, which caused the droplet to migrate from the hydrophobic side to the hydrophilic side. When the droplet reached the hydrophilic side (Fig. 4E(b2)), it was transported to the hydrophilic layer by the forces of CF, HP and HF. Finally, the droplets were dispersed by the cooperative action of CF and HP (Fig. 4E(b3)). The unidirectional transport of droplets was mainly driven by the membrane's surface properties, with gravity having minimal impact; thus, we ignored its effect.[32,33] When water droplets falling on the hydrophilic resin, it caused CF to spread the water across its surface (Fig. 4E(c1)). Until the droplets reached the hydrophilic/hydrophobic interface, the HF provided by the hydrophobic layer prevented further spread of the droplets (Fig. 4E(c2)). HP and CF increase the accumulation of water on the surface of hydrophilic resin. HP and CF were insufficient to overcome the retention caused by HF. In other words, the hydrophobic layer impeded the transport of liquid.

### 3.5 Biological evaluation of personalized elastic self-pumping dressings

Evaluating the cytocompatibility of these materials in skin wound environments was essential before studying their *in vivo* healing effects. Fibroblasts are essential for wound healing, synthesizing collagen and extracellular matrix proteins to aid tissue repair.[34] The cytotoxicity of LD@PU-A double-layer self-pumping of NIH 3T3 cells *in vitro* was evaluated using the MTT assay and the live/dead assay. As shown in Fig. 5A, concentrations of up to 50 μg $mL^{-1}$ of the four LD@PU-A extracts exhibited relatively low cytotoxicity against NIH 3T3 cells, with cell viability remaining above 75%. However, a concentration of 50 μg $mL^{-1}$ of the LD extract exhibited the lowest toxicity to NIH3T3 cells, resulting in a cell survival rate of 95.3%. Similar results were observed in the staining tests of both living and dead cells (Fig. 5B and Fig. S9†). We performed a double staining of NIH3T3 cells using calcein-AM (green, indicating living cells) and propidium iodide (PI, red, indicating dead cells) simultaneously (calcein/PI staining) to assess cell viability.[35] The results indicated that the NIH 3T3 cells on the surfaces of LD, LD@PU-A-1.2, and LD@PU-A-8.8 were stained green by calcitonin-AM. The NIH 3T3 cells on the surfaces of LD@PU-A-13.3 and LD@PU-A-18.5 exhibited minimal cell death, with very few cells appearing red. These results indicate that the LD@PU-A double-layer self-pumping dressing exhibits excellent biocompatibility and has the potential to be used as an effective wound dressing.

To demonstrate the wound healing efficacy of the LD@PU-A-13.3 self-pumping dressing *in vivo*, a circular full skin defect wound model with a diameter of 5 mm (Fig. S10†) was constructed on the dorsum of healthy C57BL/6 mice to investigate the wound healing efficiency in the following three groups: control (i), PU-A-13.3 nanofiber dressing (ii), and LD@PU-A-13.3 self-pumping dressing (iii). The wounds on the mice were monitored using a camera for a duration of 0 to 14 days and the remaining wound area decreased as the days progressed (Fig. 5C). At day 7 post-surgery, it was clearly observed that the healing degrees of wounds treated with the PU-A-13.3 nanofiber dressing (ii) and the LD@PU-A-13.3 self-pumping dressing (iii) were higher than those treated with the control group (i), and crusting was observed on all wounds. The remaining wound areas for groups (i), (ii) and (iii) were 85.3%, 64.1%, and 39.7%, respectively (Fig. 5F). It is worth noting that the scab in the wound treated with the LD@PU-A-13.3 self-pumping dressing (iii) has partially fallen off. After 14 days of treatment, scabs were still present at the wound site in both the control group (i) and the PU-A-13.3 nanofiber dressing (ii) group, and the remaining wound areas were 49.8% and 30.7%, respectively. However, the wound treated with the LD@PU-A-13.3 self-pumping dressing (iii) exhibited the most significant healing, as the scab fell off and the remaining wound area was 23.9%. Both groups (ii) and (iii) demonstrated accelerated wound healing, which may be attributed to (1) the capacity of the AgNP-containing wound dressing to protect the wound from bacterial infection and promote tissue regeneration.[36,37] (2) The "unidirectional transport" capability of the LD@PU-A-13.3 self-pumping dressing (iii) cleanses excess wound exudate and creates a favorable environment for wound healing. (3) The LD@PU-A-13.3 self-pumping dressing (iii) over the damaged skin offers appropriate mechanical support and structural cues essential for effective wound healing.[38]

Since re-epithelialization and granulation tissue formation are critical factors in evaluating the extent of wound healing, we conducted H&E staining and Masson's trichrome staining on three groups of wound tissue sections at day 14 (Fig. 5D). The LD@PU-A-13.3 self-pumping dressing (iii) group exhibited nearly complete healing of the postoperative wound epithelium and the epidermal thickness was comparable to that of normal tissue. In contrast, the control group (i) and the PU-A-13.3 nanofiber dressing group (ii) exhibited swelling in the wounds due to unexfoliated crusts, showing a significant difference in tissue thickness compared to normal tissue (Fig. 5G). In addition, Masson's trichrome staining can color the collagen in traumatic tissue blue and other cellular structures red (Fig. 5E). The LD@PU-A-13.3 self-pumping dressing (iii) group produced a greater amount of collagen in the granulation tissue compared to the control (i) and PU-A-13.3 nanofiber dressing (ii) groups and exhibited the shortest granulation tissue gap distance (Fig. 5H). We further validated the therapeutic efficacy using burn wound models (Fig. S11†). The LD@PU-A dressing demonstrated superior performance in pro-

 

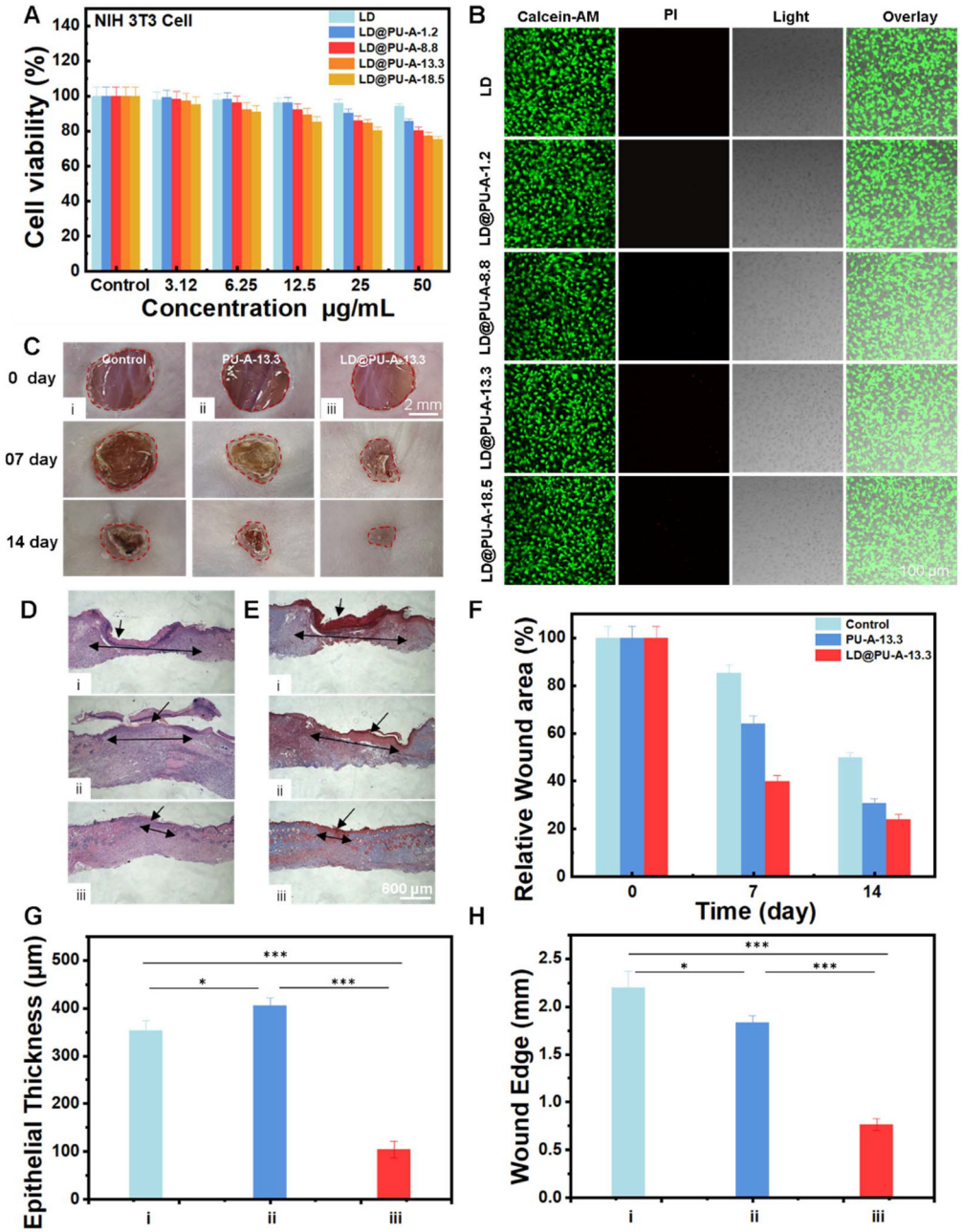


**Fig. 5** Assessment of the cytocompatibility of the PH3D@PU-A bilayer self-pumping dressing *in vitro* and the ability of the dressing to heal wounds *in vivo*. (A) MTT assay of the cell viability. (B) Representative fluorescence staining images of NIH 3T3 cells treated with LD, LD@PU-A-8.8, LD@PU-A-13.3 and LD@PU-A-18.5. (C) Promotion of wound healing by the self-pumping dressings *in vivo*. Representative images of the wounds following surgery (0 d) and after 7 d or 14 d of treatment with the control (i), the PU-A-13.3 nanofiber dressing (ii), and the LD@PU-A-13.3 self-pumping dressing (iii). The dashed boxes (added in the figure) highlight the residual wound regions that remained unhealed. Images of H&E- (D) and Masson (E)-stained trabecular tissue at day 14. The single arrow indicates the newborn epidermis and the double arrow indicates the granulation tissue gap distance. (F) Relative wound area from day 0 to day 14. Quantification of the epithelial thickness (G) and wound edge (H) on day 14. The results in all histograms are expressed as the mean ± S.D. ($n$ = 6); *$p$ < 0.05, **$p$ < 0.01 and ***$p$ < 0.001.

moting healing in burn wounds. These results suggest that the excellent wound healing effect of the LD self-pumping dressings may be attributed to the synergistic effect of the antimicrobial properties of AgNPs, the "unidirectional transport" self-cleaning properties, and the appropriate mechanical support properties, thus contributing to wound healing.

## 4. Discussion

This study demonstrates the development of a 3D-printed self-pumping dressing capable of unidirectional fluid transport and personalized customization. By integrating a hydrophilic patch with adjustable kirigami-inspired structures and a

hydrophobic nanofiber layer, the dressing extends the functionality of traditional unidirectional transport systems. It meets the demands of dynamic environments, such as wound sites near joints, by maintaining fluid drainage, antibacterial performance, and mechanical adaptability under motion (Fig. S12†). Unlike conventional unidirectional transport systems, which often rely on static designs, the use of 3D printing allows the creation of tailored structures with precise control over elasticity, stiffness, and shape (Fig. S13 and 14†). This capability significantly broadens the applicability of unidirectional fluid transport mechanisms, making them suitable for more complex anatomical regions and challenging use cases, such as retractable wounds on high-motion body parts. By offering on-demand customization, this work provides a scalable solution to meet diverse clinical needs.

Besides, we could address several key limitations to further enhance its clinical applicability. Expanding the material options, such as integrating hydrogels with tunable properties or bioactive polymers, would enable multifunctionality, including infection prevention and wound monitoring. Future designs should also explore more complex geometries through advanced 3D printing techniques to meet diverse anatomical and mechanical demands. Improving the breakthrough pressure, particularly for high-exudate or mechanically stressed wounds, remains essential, achievable by refining pore structures and layer compositions.

## 5. Conclusion

In conclusion, a personalized large-deformation self-pumping dressing was successfully developed by uniformly attaching hydrophobic antibacterial nanofibers to a hydrophilic 3D large-deformation layer. First, the fiber morphology was optimized to produce hydrophobic nanofibers with a smooth surface, uniform diameter, and evenly distributed AgNPs. Additionally, by adjusting the fundamental parameters of the large-deformation 3D-printed layer *via* computational design, the dressing was customized to achieve specific deformation and elasticity properties. Our findings demonstrate that these personalized large-deformation self-pumping dressings are suitable for various wound shapes, including retractable wounds, and effectively enable unidirectional tissue fluid transfer while promoting wound healing. This work expands the applications of electrospinning and 3D printing technologies, presenting a novel approach for the development of personalized and precise medical solutions for wound care.

## Author contributions

Zhen Gu: conceptualization, data curation, formal analysis, investigation, methodology, validation, visualization, and writing – original and review. Siyang Cheng: data curation, formal analysis, investigation, methodology, validation, and visualization. Zhe Huang: data curation, formal analysis, investigation, methodology, validation, and visualization. Heng An: data curation, formal analysis, investigation, validation, and visualization. Liping Zhou: conceptualization, resources, and writing – review and editing. Yongqiang Wen: conceptualization, co-supervision, funding acquisition, resources, and writing – review and editing.

## Data availability

All data that support the findings of this study are included within the article (and any supplementary files).

## Conflicts of interest

There are no conflicts of interest.

## Acknowledgements

This work was supported by the National Natural Science Foundation of China (T2222029, U21A20396, 52273120, and 21975019), the CAS Project for Young Scientists in Basic Research (YSBR-012), the Incubation Foundation of Beijing Institute for Stem Cell and Regenerative Medicine (2022FH125 and 2023FH122), the China Scholarship Council (No. 202206465017), the Fundamental Research Funds for the Central Universities (FRF-BR-23-02B), and the Strategic Priority Research Program of the Chinese Academy of Sciences (XDA16020802).

## References

1 Y. Y. Liu, X. Liu, H. T. Guo, X. H. Wang, A. L. Li, D. Qiu and Q. Gu, *Mater. Today Bio*, 2024, **24**, 100899.
2 S. Gong, Y. Lu, J. L. Yin, A. Levin and W. L. Cheng, *Chem. Rev.*, 2024, **124**, 455–553.
3 W. Xiao, X. Wan, L. Shi, M. Ye, Y. Zhang and S. Wang, *Adv. Mater.*, 2024, **36**, 2401539.
4 B. B. Zhang, J. Y. Li, J. K. Zhou, L. Chow, G. Y. Zhao, Y. Huang, Z. Q. Ma, Q. Zhang, Y. W. Yang, C. K. Yiu, J. Li, F. Chun, X. C. Huang, Y. Y. Gao, P. C. Wu, S. X. Jia, H. Li, D. F. Li, Y. M. Liu, K. M. Yao, R. Shi, Z. L. Chen, B. L. Khoo, W. Q. Yang, F. Wang, Z. J. Zheng, Z. K. Wang and X. E. Yu, *Nature*, 2024, 84–92.
5 Q. Shen, Y. Jiang, S. Z. Guo, L. Huang, H. B. Xie and L. Li, *J. Membr. Sci.*, 2022, **644**, 10.
6 J. Wu, N. Wang, L. Wang, H. Dong, Y. Zhao and L. Jiang, *Soft Matter*, 2012, **8**, 5996–5999.
7 X. J. Kuang, Z. F. Zhang, X. T. Ma, L. F. Zhu, Y. T. Li, P. Li, Y. Fu, T. Y. Ma, H. J. He, S. Ramakrishna and P. B. Ma, *Adv. Funct. Mater.*, 2024, **34**, 28.
8 X. D. Zhang, L. F. Li, J. Ouyang, L. Q. Zhang, J. J. Xue, H. Zhang and W. Tao, *Nano Today*, 2021, **39**, 101196.

 

9 L. X. Shi, X. Liu, W. S. Wang, L. Jiang and S. T. Wang, *Adv. Mater.*, 2019, **31**, 1804187.
10 Z. Y. Ge, W. S. Guo, Y. Tao, H. X. Sun, X. Y. Meng, L. Y. Cao, S. G. Zhang, W. Y. Liu, M. L. Akhtar, Y. Li and Y. K. Ren, *Adv. Mater.*, 2023, **35**, 14.
11 R. Z. Luo, Y. Liang, J. R. Yang, H. Q. Feng, Y. Chen, X. P. Jiang, Z. Zhang, J. Liu, Y. Bai, J. T. Xue, S. Y. Chao, Y. Xi, X. Q. Liu, E. G. Wang, D. Luo, Z. Li and J. P. Zhang, *Adv. Mater.*, 2023, **35**, 2208395.
12 Y. Yang, R. Z. Luo, S. Y. Chao, J. T. Xue, D. J. Jiang, Y. H. Feng, X. D. Guo, D. Luo, J. P. Zhang, Z. Li and Z. L. Wang, *Nat. Commun.*, 2022, **13**, 13.
13 Y. Shan, L. Xu, X. Cui, J. Zhang, H. Ouyang, X. Wang, J. Huang, J. Xue, K. Wang, D. Wang, E. Wang, K. Ren, D. Luo and Z. Li, *Cell Biomater.*, 2025, **1**, 100006.
14 A. K. Brooks, S. Chakravarty, M. Ali and V. K. Yadavalli, *Adv. Mater.*, 2022, e2109550.
15 L. Y. Daikuara, X. F. Chen, Z. L. Yue, D. Skropeta, F. M. Wood, M. W. Fear and G. G. Wallace, *Adv. Funct. Mater.*, 2022, **32**, 2105080.
16 S. Gantenbein, E. Colucci, J. Kach, E. Trachsel, F. B. Coulter, P. A. Ruhs, K. Masania and A. R. Studart, *Nat. Mater.*, 2023, **22**, 128–134.
17 T. C. Shyu, P. F. Damasceno, P. M. Dodd, A. Lamoureux, L. Z. Xu, M. Shlian, M. Shtein, S. C. Glotzer and N. A. Kotov, *Nat. Mater.*, 2015, **14**, 785–789.
18 R. Z. Luo, B. J. Shi, D. Luo and Z. Li, *Sci. Bull.*, 2023, **68**, 1740–1743.
19 L. Cheng, Z. Zhuang, M. Yin, Y. Lu, S. Liu, M. Zhan, L. Zhao, Z. He, F. Meng, S. Tian and L. Luo, *Nat. Commun.*, 2024, **15**, 9786.
20 L. Shi, X. Liu, W. Wang, L. Jiang and S. Wang, *Adv. Mater.*, 2019, **31**, 1804187.
21 T. Min, X. Sun, Z. Yuan, L. Zhou, X. Jiao, J. Zha, Z. Zhu and Y. Wen, *LWT*, 2021, **135**, 110034.
22 L. Shi, X. Liu, W. Wang, L. Jiang and S. Wang, *Adv. Mater.*, 2019, **31**, e1804187.
23 I. Pastoriza-Santos and L. M. Liz-Marzán, *Pure Appl. Chem.*, 2000, **72**, 83–90.
24 Z. Zhang, L. Zhang, S. Wang, W. Chen and Y. Lei, *Polymer*, 2001, **42**, 8315–8318.
25 Y. Zhao, H. Wang, H. Zhou and T. Lin, *Small*, 2017, **13**, 1601070.
26 A. Sobhan, K. Muthukumarappan, L. Wei, T. Van Den Top and R. Zhou, *Mater. Today Commun.*, 2020, **23**, 2352–4928.
27 F. Bao, G. Pei, Z. Wu, H. Zhuang, Z. Zhang, Z. Huan, C. Wu and J. Chang, *Adv. Funct. Mater.*, 2020, **30**, 2005422.
28 L. Qi, K. Ou, Y. Hou, P. Yuan, W. Yu, X. Li, B. Wang, J. He, S. Cui and X. Chen, *Mater. Des.*, 2021, **201**, 109461.
29 Y. S. Guan, Z. Zhang, Y. Tang, J. Yin and S. Ren, *Adv. Mater.*, 2018, **30**, e1706390.
30 T. Guo, K. Han, L. Heng, M. Cao and L. Jiang, *RSC Adv.*, 2015, **5**, 88471–88476.
31 D. Miao, Z. Huang, X. Wang, J. Yu and B. Ding, *Small*, 2018, **14**, e1801527.
32 H. Zhou, H. Wang, H. Niu and T. Lin, *Sci. Rep.*, 2013, **3**, 2964.
33 M. Cao, J. Xiao, C. Yu, K. Li and L. Jiang, *Small*, 2015, **11**, 4379–4384.
34 H. An, M. Zhang, L. P. Zhou, Z. Huang, Y. C. Duan, C. Wang, Z. Gu, P. X. Zhang and Y. Q. Wen, *Adv. Funct. Mater.*, 2023, **33**, 202211182.
35 Y. Li and X. Han, *Environ. Toxicol. Pharmacol.*, 2012, **33**, 318–326.
36 A. GhavamiNejad, A. R. Unnithan, A. Ramachandra, M. Samarikhalaj, R. G. Thomas, Y. Y. Jeong, S. Nasseri, P. Murugesan, D. Wu, C. H. Park and C. S. Kim, *ACS Appl. Mater. Interfaces*, 2015, **7**, 12176–12183.
37 Z. Jia, P. Xiu, M. Li, X. Xu, Y. Shi, Y. Cheng, S. Wei, Y. Zheng, T. Xi, H. Cai and Z. Liu, *Biomaterials*, 2016, **75**, 203–222.
38 Z. Yuan, K. Zhang, X. Jiao, Y. Cheng, Y. Zhang, P. Zhang, X. Zhang and Y. Wen, *Biomater. Sci.*, 2019, **7**, 5084–5096.